Monthly Notices
of the
ROYAL ASTRONOMICAL SOCIETY

MNRAS **491,** 4069–4075 (2020)
Advance Access publication 2019 November 14

doi:10.1093/mnras/stz3172

VLBI observations of the G25.65+1.05 water maser superburst

R. A. Burns [1,2,3★] G. Orosz [4,5] O. Bayandina [1,6] G. Surcis,[7] M. Olech,[8] G. MacLeod,[9,10] A. Volvach,[6,11] G. Rudnitskii,[12] T. Hirota,[2] K. Immer,[1] J. Blanchard,[1,13] B. Marcote [1] H. J. van Langevelde,[1,14] J. O. Chibueze,[15,16] K. Sugiyama,[2,17] Kee-Tae Kim,[3,18] I. Val'tts,[6] N. Shakhvorostova,[6,19] B. Kramer,[17,20] W. A. Baan [5,21] C. Brogan,[22] T. Hunter,[22] S. Kurtz,[23] A. M. Sobolev [19] J. Brand [24] and L. Volvach[6,11]

Affiliations are listed at the end of the paper

Accepted 2019 November 8. Received 2019 November 7; in original form 2019 March 28

ABSTRACT

This paper reports observations of a 22 GHz water maser 'superburst' in the G25.65+1.05 massive star-forming region, conducted in response to an alert from the Maser Monitoring Organisation (M2O). Very long baseline interferometry (VLBI) observations using the European VLBI Network (EVN) recorded a maser flux density of 1.2×10^4 Jy. The superburst was investipgated in the spectral, structural, and temporal domains and its cause was determined to be an increase in maser path length generated by the superposition of multiple maser emitting regions aligning in the line of sight to the observer. This conclusion was based on the location of the bursting maser in the context of the star-forming region, its complex structure, and its rapid onset and decay.

Key words: masers – techniques: high angular resolution – stars: individual: G25.65+1.05 – stars: massive.

1 INTRODUCTION

Galactic maser emission is predominantly associated with the births and deaths of stars. At radio frequencies their uses as astrophysical tools are numerous; revealing milliarcsecond (mas) scale structures and three-dimensional motions in the smallest, densest regions of activity (Moscadelli et al. 2016; Moscadelli, Sanna & Goddi 2018) that are typically inaccessible to other wavelengths. Despite a heavy reliance on their functionality, the mechanisms of certain maser behaviours remain to be fully explained, particularly their temporal flux variability.

'Maser burst' and 'maser flare' are both terms that have been used in recent literature to describe a sudden increase in the intensity of maser emission. We emphasize that the term 'maser burst' in this paper is employed to this same meaning and does not refer to an accretion burst, or any other physical 'burst'. The term 'superburst' refers to a particularly extreme class of maser bursts, where a maser emitting region exhibits a sudden increase in flux density of several orders of magnitude. There are three recognized water maser superburst star-forming regions (SFRs): Orion KL (Matveenko, Graham & Diamond 1988; Garay, Moran & Haschick 1989; Shimoikura et al. 2005; Hirota et al. 2011, 2014a), W49N (Honma et al. 2004; Kramer, Menten & Kraus 2018; Volvach et al. 2019c), and G25.65+1.05 (Ashimbaeva et al. 2017; Volvach et al. 2017, 2019b). Sudden enhancement in maser flux density, though less extreme, has also been seen in species other than water (MacLeod et al. 2018; Szymczak et al. 2018) and in evolved stars (Esipov et al. 1999; Vlemmings et al. 2014; Gómez et al. 2015; Etoka et al. 2017).

Superbursts are both rare and transient in nature and consequently their mechanism of action remains enigmatic. The widely cited Deguchi & Watson (1989) model generally allows for three avenues of flux enhancement of maser emission: an increase in the incident continuum photon flux being amplified; mechanical/radiative induction of more favourable maser pumping conditions; or an increase in the path length of the maser cloud along the line of sight to the observer.

These different burst scenarios associate specifically to a variety of spatial and physical scenarios that help to place constraints on our understanding of the local medium. Superbursts therefore represent an avenue to investigate the nature of maser emission under atypical circumstances, exposing amplification conditions.

G25.65+1.05, hereafter G25, is a region of massive star formation that recently achieved notoriety due to its recurring maser burst behaviour, exhibiting kJy bursts on several occasions (Lekht et al. 2018; Volvach et al. 2019a,b). The source distance is disputed, with estimates ranging from 2.7 kpc (Sunada et al. 2007) to 12.5 kpc (Green & McClure-Griffiths 2011), with the latter value making G25 the most powerful maser in the Galaxy (Volvach et al. 2019a).

★ E-mail: rossburns88@googlemail.com

© 2019 The Author(s)
Published by Oxford University Press on behalf of the Royal Astronomical Society

Downloaded from https://academic.oup.com/mnras/article/491/3/4069/5625785 by INAF Cagliari (Osservatorio Astronomico di Cagliari) user on 19 April 2021

In this paper, we introduce new very long baseline interferometry (VLBI) observations targeting the superburst activity of water maser emission in G25. We investigate the bursting mechanism by structural analyses of individual maser features; the overall distribution of masers in the context of the star-forming region; and maser temporal behaviour via cross-matching VLBI spatial maser features with spectral maser features from historic and recent single-dish monitoring campaigns. Our discussion builds on the context set out in the Very Large Array (VLA) observations made on the 2017 December 9, described in Bayandina et al. (2019b), whose work serves as a basis for forthcoming studies of the G25 water maser.

2 OBSERVATIONS AND DATA REDUCTION

Target of Opportunity (ToO) observations of the water maser in G25 were requested to the European VLBI Network (EVN) in response to the 2017 September burst activity reported by the single-dish Maser Monitoring Organisation (M2O,[1] a global cooperative of maser monitoring programs). Six stations were able to respond to the ToO request: Effelsberg, Jodrell Bank (Mark II), Onsala (20 m), Toruń, Yebes, and Hartebeesthoek. Observations were carried out on the 2017 October 2 in eVLBI mode whereby locally time-stamped, DBBC8 filtered data are transferred directly to the SFXC correlator at Joint Institute for VLBI in Europe (JIVE; Keimpema et al. 2015). This approach circumvents data shipping delays and thus enables quicker evaluation of transient events.

Data were transferred at 128 Mbps, comprising one single 16-MHz frequency band with 2-bit Nyquist sampling and dual circular polarizations. Bands were centred at the rest frequency of the water maser, 22.235080 GHz. Correlated data were generated with 8192 frequency channels to provide 2 kHz channel separation, equivalent to 0.03 km s^{-1}.

Using this set-up, the array observed M87 for 1 h preceding the main science programme in order to synchronize the eVLBI data streams of participating stations to within ∼16 μs. G25 was observed in 30 min scans, breaking at the 12 and 18 min marks for Tsys calibration of <15 s duration. At each hour J2202+4216 (BL Lac) was observed as a delay, bandpass, and polarization calibrator. We also included two 10-min scans each of DA553 and 4C075 for electric vector position angle (EVPA) calibration and check. W49N and J1905+0952 were also observed – these data, and the polarization results for G25, will be presented in forthcoming works. The scheduled observing time was 14 h, of which G25 was scheduled for 3.26 h.

Fringes to all stations were obtained except for the left circular polarization data from Toruń. An issue with the VLBI firmware affecting the last EVN sessions of 2017 and first session of 2018 lead to erroneous amplitudes across participating stations. We discuss efforts to circumvent this issue below. Data products were processed to FITS files at JIVE[2] and are publicly available from the EVN archive under observation code RB004.

2.1 Data reduction

Primary calibration was carried out using the AIPS[3] software package. Station-based flags, bandpass, and gain calibration tables produced by the EVN data reduction pipeline were sourced from the online archive and appended to the main data set. These calibration tables also include a priori ionospheric, correlator sampler, and parallactic angle corrections. Delay and bandpass solutions were derived using J2202+4216 and applied to all sources. The aforementioned amplitude issue was circumvented by scaling the observed flux density of J2202+4216 based on independent VLBI K-band measurements from the Gamma-ray Emitting Notable AGN Monitoring by Japanese VLBI (GENJI) monitoring project (Nagai et al. 2013).

Dispersive phase and rate variations, dominated by tropospheric fluctuations, were corrected by fringe fitting on a reference maser with a peak flux density of 409 Jy and simple, unresolved emission, inferred from its constant flux density as a function of projected baseline length.

After applying all phase and gain calibrations to the full spectral line data set, small shifts were made in the frequency domain to account for time-dependent Doppler shifts caused by Earth rotation. Finally, an image cube was produced for spectral line channels in a +35 to +55 km s^{-1} velocity range, covering a region of 1.4 × 1.4 arcsec^2 based on the VLA maser maps of Bayandina et al. (2019b). The synthesized beam had dimensions of 1.2 × 0.7 mas, with a position angle of 81° measured anticlockwise from north. The similarity of the cross-power spectrum evaluated within the primary beam (POSSM) with a spectrum evaluated using only the emission in our mapped region (ISPEC) indicated that most of the emission had been successfully included in the map.

The final image cube was searched for emission exceeding a signal-to-noise ratio cut-off of 7 for the majority of the map, however, a higher cut-off value of 100 was necessary for bright maser channels with elevated image noise due to dynamic range limiting. Henceforth, a maser 'spot' refers to emission, per channel, originating from a maser cloud. All flux densities discussed in this paper, including single-dish measurements, are subject to a 10 per cent absolute calibration uncertainty.

3 RESULTS

3.1 Spectral distribution of masers in G25

The 22 GHz water maser spectrum measured by the EVN is shown in Fig. 1 (black solid line). Masers were detected in the range of $+35 < v_{\rm LSR} < +55$ km s^{-1} with the bursting maser occurring at $v_{\rm LSR} = +42.9$ km s^{-1}, i.e. close to the central velocity of the spectral features. Molecular line observations place the systemic velocity of G25 at $v_{\rm LSR} \sim +42$ km s^{-1} (Bronfman, Nyman & May 1996; Molinari et al. 1996) thus masers in G25 exhibit only modest velocities in the line-of-sight direction.

Fig. 1 also shows single-dish spectra during and prior to the 2017 September superburst; the EVN detected all spectral features in G25 and the number of spectral components remains constant in time. Significant temporal changes in flux were exclusive to the bursting feature that increased from 10^2 Jy in the quiescent phase to 10^4 Jy in the superburst phase. In contrast to the superburst feature, the profile of the feature at +37 km s^{-1} remained constant across all observations while only small changes were seen in the +50 to +55 km s^{-1} range, as is shown in the lower panel of Fig. 1.

3.2 Spatial distribution of masers in the G25 SFR

The VLBI maser spot map is shown in Fig. 2. The majority of maser emission in G25 resides in the form of two arc structures: an east–

[1] masermonitoring.org
[2] Joint institute for VLBI ERIC, http://www.jive.nl.
[3] Astronomical Image Processing System, www.aips.nrao.edu.

Downloaded from https://academic.oup.com/mnras/article/491/3/4069/5625785 by INAF Cagliari (Osservatorio Astronomico di Cagliari) user on 19 April 2021

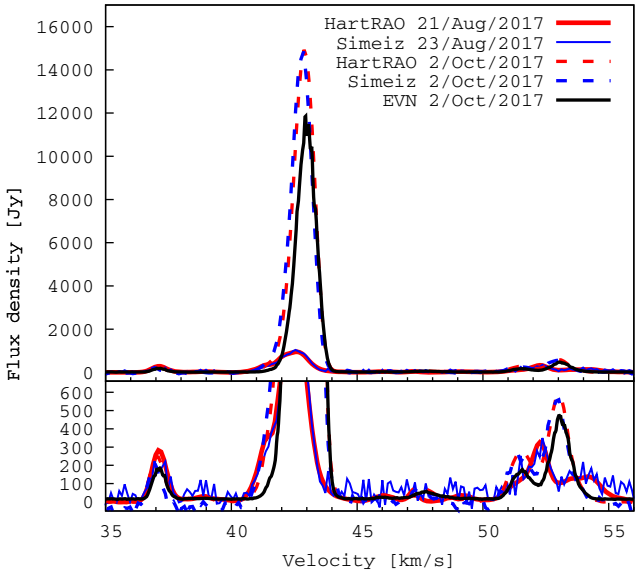


Figure 1. The scalar averaged, cross-power water maser spectrum measured with the European VLBI Network (EVN; solid, black line) is shown in comparison to single-dish spectra provided by the Maser Monitoring Organisation (M2O) on the same date (dashed red and blue lines) and pre-flare (solid red and blue lines). The panel below highlights the low flux density maser features.

west (E–W)-orientated arc near $(x,y) = (0,0)$ mas offset that contains the bursting feature at the arc centre, and a north-east–south-west (NE–SW) arc near $(x,y) = (350, -1000)$ mas offset (Fig. 2, right). These arcs coincide with the two brightest radio continuum sources in G25: VLA 1 and VLA 2 (see Fig. 3). We henceforth adopt these names for the maser arcs in relevant discussion below. Masers associated with VLA 1 exhibit the full range of velocity components, +35 to +55 km s^{-1}, while masers associated with VLA 2 were typically in the range of +35 to +40 km s^{-1}. Maser spots were also observed in the region between VLA 1 and VLA 2, these masers were closer in velocity to the VLA 2 group.

3.3 Flux density and the structure of masers in G25

The highest flux density measured by the EVN was 1.2×10^4 Jy (Fig. 1; Fig. 2, left). Fig. 1 shows a comparison of the EVN cross-correlation flux density, which is sensitive only to the milliarcsecond scale, to spectra measured independently by single-dish instruments at the Hartebeesthoek Radio Astronomy Observatory (HartRAO) and Simeiz Radio Observatory (Volvach et al. 2019b) that are sensitive to emission on all angular scales within the primary beam (a few arcmin). A comparison of the peak flux densities reported by HartRAO, 1.5×10^4 Jy, and Semiez, 1.5×10^4 Jy, with that of the EVN, 1.2×10^4 Jy, reveals that 80 ± 10 per cent of the bursting maser flux emanates from the milliarcsecond scale, i.e. the superburst maser emission in G25 is highly compact. Similarly high percentage flux recovery was observed for non-bursting maser features indicating that most masers in G25 are highly compact. The EVN did not completely recover all maser emission from the 'blue' side of bursting feature (around +41 km s^{-1}, Fig. 1) indicating that the emission is extended.

Two kinds of complex structure were found in the EVN observations of the bursting spectral component. First, emission in the brightest spectral channel exhibited two-scale structure comprising both compact and an extended emission (Fig. 4, right). Secondly, when imaging the lower flux channels of the superburst spectral feature, the maser emission was seen to decompose into two spatially distinct peaks in the blue wing limit (Fig. 4, left). Each of these characteristics is discussed in the following subsections.

3.4 Compact and extended emission

Structural analysis of maser emission in interferometric data is possible via consideration of the flux density as a function of projected baseline length. A constant visibility amplitude with increasing baseline length in such a plot indicates emission that is unresolved on all baselines, as was the case for the reference maser on which the phase calibration was based. On the other hand, a decreasing visibility amplitude with baseline length indicates that emission is partially resolved out on the longer baselines. The lack of intermediate-length baselines between the continental and intercontinental EVN stations hinders an in-depth structural analysis, however, some basic assertions can be made. Fig. 4 (right) reveals that the superburst maser component in G25 is partially resolved, with emission on two spatial scales: a mas-scale component of $\sim 1.0 \times 10^4$ Jy and a sub-milliarcsecond component of $\sim 4.0 \times 10^3$ Jy. These correspond to brightness temperature lower limits of 4.7×10^{13} and 2.0×10^{14} K, respectively.

The visibility data sampled at the peak flux channel were best fit by a linear structure whose flux profile is a Gaussian of 0.3 mas full width at half-maximum, at a position angle (PA) of 115°. Note that the elongation of emission is markedly different from the PA of the synthesised beam (81°), ruling out beam effects. The maser data and linear model are shown as functions of projected baseline length in Fig. 4 (right).

3.5 Decomposition of the blue wing

The spectral profile of the bursting maser feature revealed significant excess flux in the blue wing near +41 km s^{-1}, which is especially visible when viewed in log scale in Fig. 4 (middle). The channels comprising this blue wing were imaged and the corresponding channel maps are shown in Fig. 4 (left). The maps reveal complex structure in the blue wing of the G25 superburst maser feature delineating a clear decomposition into two spatially distinct maser features at a north-west–south-east (NW–SE) PA, specifically PA $\simeq 115°$.

4 DISCUSSION

For in-depth discussions on astrophysical masers the reader may refer to Deguchi & Watson (1989), Elitzur, McKee & Hollenbach (1991), Gray (1999, 2012), and Sobolev & Gray (2012). We only list here some of the key properties of maser emission that should be considered when interpreting the maser superburst presented in this paper.

4.1 Possible routes of the superburst mechanism

Masers are the product of stimulated emission in which an incident photon (from the local environment or from background radiation) initiates an exponentially proliferating de-excitation cascade; each input photon leading to two output photons for each occurrence of stimulated emission. This behaviour is sustained providing the existence of a sufficient pool of excited molecules to de-excite, i.e.

Downloaded from https://academic.oup.com/mnras/article/491/3/4069/5625785 by INAF Cagliari (Osservatorio Astronomico di Cagliari) user on 19 April 2021

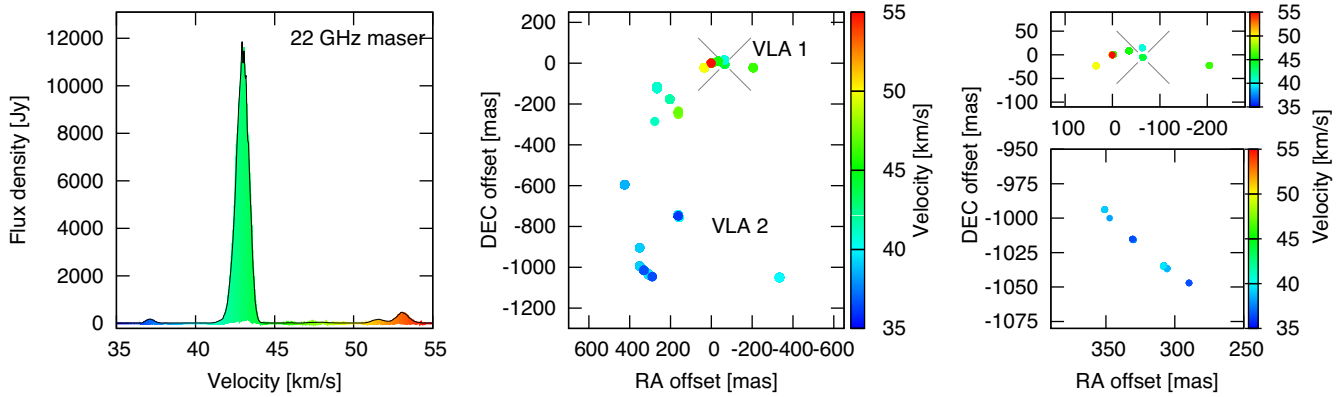


Figure 2. Left-hand panel shows the scalar averaged spectrum of maser emission in G25. Middle panel shows the spatial distribution of maser spots in G25. Right-hand panels show blow-ups of the arc structures near VLA 1 and VLA 2, above and below, respectively. The superburst maser is identified with a cross. In all subplots colours indicate local standard of rest (LSR) velocity.

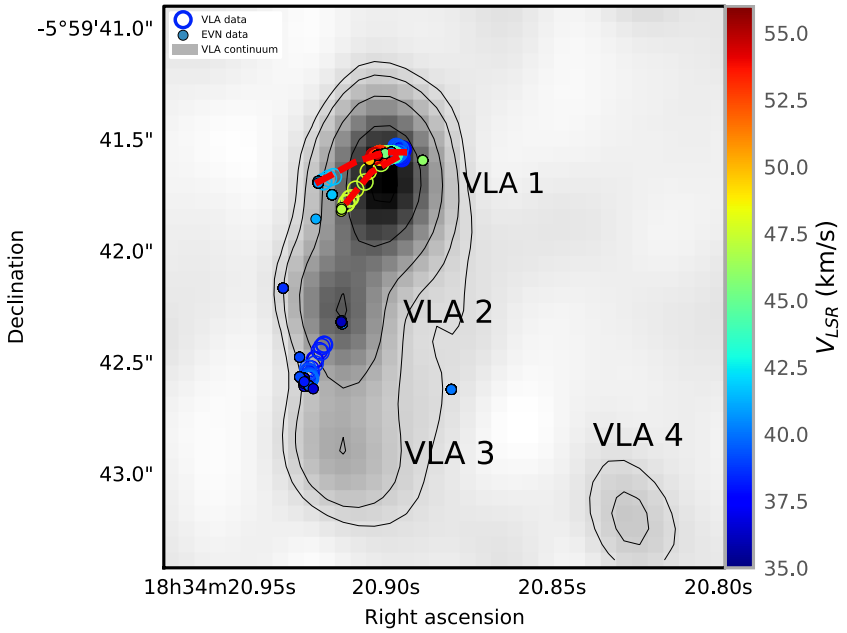


Figure 3. Visual summary of the water maser and 22 GHz continuum emission in G25, comparing results from this work with VLA data from Bayandina et al. (2019b) taken on the 2017 December 9, from which the continuum sources VLA 1, 2, 3, and 4 are labelled. Open circles indicate maser emission detected by the VLA, while filled circles represent masers from this work. Colours indicate line of sight velocity and the red dashed line delineates the lateral 'V' discussed in Section 5.

the rate of populating the excited state(s) must be faster than the rate of de-excitation; the maser is then said to be 'unsaturated'. When de-excitation surpasses excitation rates the maser can no longer amplify with an exponential relation to the maser path length and the maser is said to be 'saturated'.

The three key factors influencing the observed maser output are therefore the intensity of incident emission, the abundance of population-inverted molecules, and the number of de-excitable molecules along the observer's line of sight. As such, these form the three general routes considered in explaining the superburst mechanism. Discerning which of these factors is responsible for the superburst observed in G25 is possible by noting some distinguishable observational signatures.

In the case of an increase in incident photons, all maser emitting gas (of any molecular species) foreground to the source of continuum emission would exhibit an enhanced flux. Masers, either compact or extended, covering a wide range of velocities may be involved, as was seen in NGC 6334I (MacLeod et al. 2018). Temporally, the maser enhancement should reflect changes in the radiation field where, in the unsaturated domain, a linear increase would lead to an exponential maser flux density increase (as was seen in Szymczak et al. 2018). In the cases of S255IR and NGC 6334I several radiation-driven maser transitions were enhanced for several weeks while some transitions remained enhanced for several years (MacLeod et al. 2018; Szymczak et al. 2018) suggestive of a lasting elevated local continuum radiation field.

In the case of water masers, enhanced pumping conditions in a shock could contribute the collisional energy required for producing population inversion of the 22 GHz water maser transition (Hollenbach, Elitzur & McKee 2013). Observationally, this would manifest as enhanced flux only for maser emitting regions proximal in location to the shocked gas, which, for proto-/stellar jets, are typically

Downloaded from https://academic.oup.com/mnras/article/491/3/4069/5625785 by INAF Cagliari (Osservatorio Astronomico di Cagliari) user on 19 April 2021

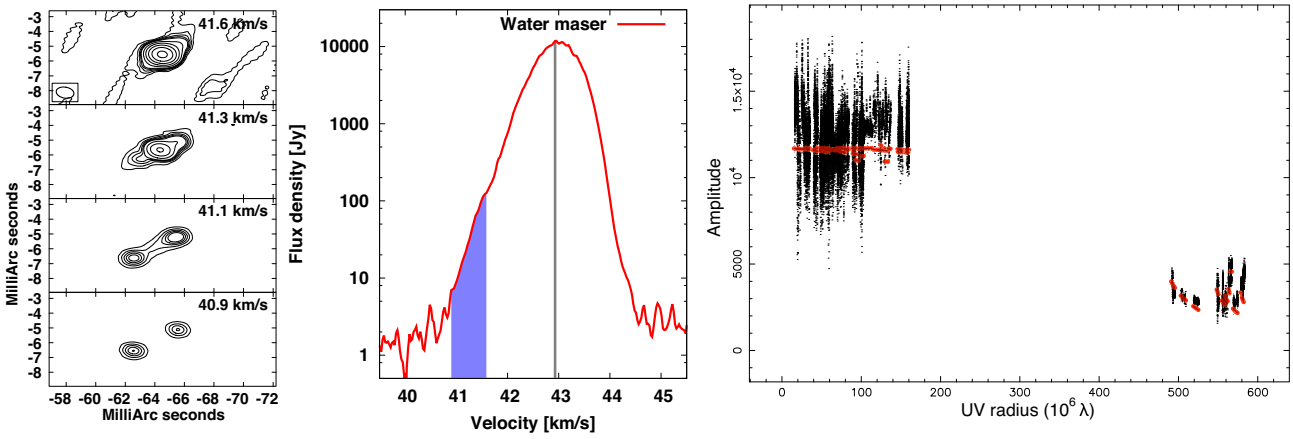


Figure 4. Middle: a logarithmic scale spectrum highlighting the bursting maser feature in which the peak channel is indicated with a grey line and the blue wing is coloured. Left: channel maps of the blue wing convey the structure of the emission with contours at 1, 2, 3, 4, 5, 10, 20, 40, 80, and 160 multiples of 0.5 Jy that is a typical 3σ noise value in the off-peak channels. Coordinates are relative to the reference maser spot. Right: a plot of amplitude as a function of projected baseline length for the peak maser channel (black) and a linear model with a Gaussian flux density profile (red) indicating structure at sub-/milliarcsecond scale.

several 100 au (e.g. Goddi, Moscadelli & Sanna 2011; Cesaroni et al. 2018). Temporally, water maser bursts associated with new shocks would depend on the balance of pumping conditions.

Occurrences of stimulated emission increase along the propagation path of the maser gas. This can occur in the case of a geometrically or structurally variable maser complex. Gray et al. (2019) show that in the case of a rotating maser cloud, quasi-periodic maser variability can be produced, however strong flaring behaviour cannot. Conversely, a significant increase in path length can also be achieved when multiple maser emitting regions producing emission at the same frequency overlap on the sky plane viewed by the observer; an effect confined to a very narrow spectral domain but not requiring association with shocks or continuum regions (e.g. Shimoikura et al. 2005). Temporally, the burst would persist as long as the alignment is maintained that would depend on the angular scale and relative motions of the individual components as viewed from the perspective of the observer. While one superburst in Orion KL lasting several hundred days was found to be associated with two overlapping maser emitting regions (Shimoikura et al. 2005), far shorter bursts of less than 2 d duration are known to have occurred in the same source (Matveenko et al. 1988). Assuming typical Galactic proper motions of several mas yr^{-1}, a maser overlap region on the order of 1/365 mas would be required to achieve temporal variability on an intraday level.

4.2 The superburst in G25

Attributing the superburst in G25 to one of the aforementioned scenarios is facilitated by considering the available observational evidence; namely, the maser structure and distribution in the context of the G25 SFR, and temporal behaviours known from historic monitoring campaigns (Lekht et al. 2018; Volvach et al. 2019b). These are each discussed below. It should also be noted that despite the high flux densities involved the masers in G25 remain unsaturated (Volvach et al. 2019a,b).

4.2.1 Spatial and environmental considerations

G25 contains four centimetre sources, VLA 1, VLA 2, VLA 3, and VLA 4, the natures of which are discussed in Bayandina et al. (2019b). VLA 2 is the only detected millimetre source in the G25 SFR and also houses class II methanol masers. It is thus likely to represent the embedded massive star that drives activity in this region. The superburst maser is located in VLA 1 (see Fig. 3, edited from Bayandina et al. 2019b) that is the brightest source of 5 cm emission in the G25 region, and, in contrast to VLA 2, exhibits no class II methanol masers or millimetre emission. VLA 1 may therefore constitute a shock region that would be consistent with the production of collisionally excited water masers.

Shocks produced in bipolar ejections from massive stars exhibit typical sizes of ∼300 au (e.g. Goddi et al. 2011; Cesaroni et al. 2018) and protostellar discs exhibit similar scales (Simon, Dutrey & Guilloteau 2000; Hirota et al. 2014b; Pérez et al. 2016). In contrast, almost all of the flux density enhancement in the G25 superburst originated from a single sub-milliarcsecond region, which is <2.7 to <12.5 au, depending on the adopted distance (2.7 or 12.5 kpc). The largest maser structure is the arc associated with VLA 1 that hosts the superburst maser feature (Fig. 3). Its 300 mas extent would correspond to 810 or 3750 au depending on adoption of the near or far distance, respectively. If the maser burst were driven by new shock energy, the confinement of the flux enhancement to one part of the arc becomes difficult to explain.

4.2.2 Temporal considerations

We can infer the historic temporal behaviour of the bursting maser feature by following the +42.8 km s^{-1} maser emission of Volvach et al. (2019b, see their fig. 2). Temporal variations in the maser flux in G25 are some of the most extreme reported in the literature, with three extreme flares occurring between 2002 and 2016 (Lekht et al. 2018), including several short, and even intraday bursts (Ashimbaeva et al. 2017; Volvach et al. 2019b). Such rapid increase and subsequent decrease time-scales are much faster than those reported in association with shocks and accretion events (MacLeod et al. 2018; Szymczak et al. 2018). As mentioned previously, assuming ∼mas yr^{-1} proper motions the intraday variability seen in G25 implies an overlap region of angular size of the order 1/365 mas. Such a compact source structure in the superburst component is supported observationally in G25 (see below).

Downloaded from https://academic.oup.com/mnras/article/491/3/4069/5625785 by INAF Cagliari (Osservatorio Astronomico di Cagliari) user on 19 April 2021

4.2.3 Structure of the superburst water maser in G25

While a comparison of single-dish and VLBI scale maser spectra (Fig. 1) reveals that 80 ± 10 per cent of the total maser emission in G25 emanates from the milliarcsecond scale, a comparison of continental and intercontinental EVN data for the +42.9 km s^{-1} channel reveals contributions to flux density on the milliarcsecond and sub-milliarcsecond scales (Fig. 4, right). The detection of the same maser feature on space VLBI baselines (Kurtz 2018; Bayandina et al. 2019a) confirms that the bursting maser feature in G25 is extremely compact.

VLBI imaging of the emission uncovered an elongation in the NW–SE direction, which was best fit by a model of a linear extension with a Gaussian flux density profile (Fig. 4, right). While a map of the emission in the blue wing of the flaring feature (around +41 km s^{-1}) revealed two spatially distinct peaks that flank the location of the flaring feature (Fig. 4, left). The NW–SE orientation of the spatially separated peaks matches the PA of the aforementioned linear model fit to the peak channel that suggests causality, implying that the superburst feature and two weaker features are associated.

5 CONCLUSION AND HYPOTHESIS

The structure and flux density profile in the bursting feature in G25 can be explained by a scenario whereby two mas-scale maser emitting regions partially overlap on the sky plane at a NW–SE orientation (see Fig. 4, left). The partial overlap forms a sub-milliarcsecond region of increased maser path length with an extension in the NW–SE as is described by the model fit to the peak maser channel (Fig. 4, right). The small angular size of this region is corroborated by detection of the same feature in space VLBI observations during the G25 superburst event, as reported by Bayandina et al. (2019a).

Here we hypothesize a scenario whereby such an overlap might occur, and why they are not more commonly observed in maser-bearing SFRs. When viewing the EVN data in the context of VLA data from Bayandina et al. (2019b), maser emission associated with VLA 1 has the morphology of a lateral 'V' shape, as can be seen in Fig. 3. The maser superburst occurred in a feature residing at the apex of the 'V'. We hypothesize that the lateral 'V' traces two linear maser associations, or 'sheets' that, from the viewpoint of the observer, intersect at a position in the sky plane corresponding to the position on the superburst maser. This overlap of maser sheets could provide an increase in the path length of maser gas as chance superpositions occur between masers in the two sheets. To achieve a colocation of *velocity coherent* maser sheets would require an alignment in both position, and line-of-sight velocity, which may explain why such events are rarely seen.

According to this hypothesis a relative proper motion between the two sheets in a general north–south (N–S) direction would cause the overlap region to propagate laterally in the sky plane, like the cross-point of an opening or closing pair of scissors. This propagation would traverse with a proper motion $\mu_{\rm cross\text{-}point} = \mu_{\rm relative}/\tan\theta$, where θ is the angle between the sheets and $\mu_{\rm relative}$ is their relative proper motion. Water masers in shocks typically move at about $v \sim 20$ km s^{-1} (Burns et al. 2016, 2017) that at distances of 2.7 and 12.5 kpc, and holding one sheet stationary, corresponds to relative proper a motion of $\mu_{\rm relative} \sim 0.3$–$1.5$ mas yr^{-1}. For $\theta \sim 20^\circ$ in VLA 1 we estimate that the cross-point in the maser sheets would propagate in the sky plane at $\mu_{\rm cross\text{-}point} \sim 0.8$–$4.1$ mas yr^{-1}. Masers in G25 typically group on ∼30 mas scales and also form milliarcsecond scale complexes (Fig. 2, right), thus our hypothesis would predict chance alignments to occur multiple times during a months-to-years scale flurry, interspersed with periods of decade-scale quiescence. This hypothesis is remarkably consistent with the long-term, high-cadence light curves of Lekht et al. (2018). Maser cloud trajectories attained via VLBI proper motion observations would provide a test of this hypothesis and possibly allow the prediction of future superbursts.

6 SUMMARY

The key points of this paper can be summarized as follows.

EVN (VLBI) data taken of a 1.2×10^4 Jy water maser superburst in G25.65+1.05 were presented, and supplemented by single-dish data from the M2O.

The superburst was investigated in the spectral, spatial, and temporal domains and the results were used to differentiate between the mechanisms of action considered feasible by basic maser theory.

The superburst feature presented an elongated structure with PA = 115°, and was flanked by two weaker, spatially separated features, their relative position angle was also PA $\simeq 115^\circ$.

VLBI and single-dish data consistently favour a scenario whereby an alignment, or 'overlap', of multiple unsaturated maser emitting regions in the sky plane produced a superburst via a sudden increase in the maser path tlength along the line of sight to the observer.

Observations locate the bursting maser feature at the intersect of two maser sheets. Multi-epoch VLBI measurements of the trajectories of maser features associated with the maser 'sheets' could allow the prediction of future maser superbursts in G25.

ACKNOWLEDGEMENTS

RAB acknowledges support through the EACOA Fellowship from the East Asian Core Observatories Association. GO acknowledges support from the Australian Research Council Discovery project DP180101061 funded by the Australian Government, the CAS 'Light of West China' Program 2018-XBQNXZ-B-021, and the National Key R&D Program of China 2018YFA0404602. TH is financially supported by the MEXT/JSPS KAKENHI Grant Number 17K05398. BM acknowledges support from the Spanish Ministerio de Economía y Competitividad (MINECO) under grants AYA2016-76012-C3-1-P and MDM-2014-0369 of ICCUB (Unidad de Excelencia 'María de Maeztu'). NS acknowledges support from Russian Science Foundation grant 18-12-00193. AMS is supported by the Ministry of Science and High Education (the basic part of the State assignment, RK No. AAAA-A17-117030310283-7) and by the Act 211 Government of the Russian Federation, contract No.02.A03.21.0006. JOC acknowledges support by the Italian Ministry of Foreign Affairs and International Cooperation (MAECI Grant Number ZA18GR02) and the South African Department of Science and Technology's National Research Foundation (DST-NRF Grant Number 113121) as part of the ISARP RADIOSKY2020 Joint Research Scheme. This work was supported by the National Science Centre, Poland through grant 2016/21/B/ST9/01455. WAB acknowledges the support from the National Natural Science Foundation of China under grant No.11433008 and the Chinese Academy of Sciences President's International Fellowship Initiative under grant No. 2019VMA0040. This work was funded by the RFBR, project number 19-29-11005. The European VLBI Network is a joint facility of independent European, African, Asian, and

Downloaded from https://academic.oup.com/mnras/article/491/3/4069/5625785 by INAF Cagliari (Osservatorio Astronomico di Cagliari) user on 19 April 2021

North American radio astronomy institutes. Scientific results from data presented in this publication are derived from the following EVN project code: RB004

We would like to thank the anonymous referee whose direction lead to crucial improvements in the scientific impact of this work, in addition to clarification of the manuscript.

REFERENCES

Ashimbaeva N. T., Platonov M. A., Rudnitskij G. M., Tolmachev A. M., 2017, Astron. Telegram, 11042
Bayandina O. S., Shakhvorostova N. N., Alakoz A. V., Burns R. A., Kurtz S. E., Val'tts I. E., 2019a, Adv. Space Res., in press
Bayandina O. S., Burns R. A., Kurtz S. E., Shakhvorostova N. N., Val'tts I. E., 2019b, ApJ, 884, 140
Bronfman L., Nyman L.-A., May J., 1996, A&AS, 115, 81
Burns R. A., Handa T., Nagayama T., Sunada K., Omodaka T., 2016, MNRAS, 460, 283
Burns R. A. et al., 2017, MNRAS, 467, 2367
Cesaroni R. et al., 2018, A&A, 612, A103
Deguchi S., Watson W. D., 1989, ApJ, 340, L17
Elitzur M., McKee C. F., Hollenbach D. J., 1991, ApJ, 367, 333
Esipov V. F., Pashchenko M. I., Rudnitskij G. M., Kozin M. V., Lekht E. E., Nadjip A. E., Fomin S. V., 1999, in Le Bertre T., Lebre A., Waelkens C., eds, Proc. IAU Symp. 191, Asymptotic Giant Branch Stars. Astron. Soc. Pac., San Francisco, p. 201
Etoka S., Gérard E., Richards A. M. S., Engels D., Brand J., Le Bertre T., 2017, MNRAS, 468, 1703
Garay G., Moran J. M., Haschick A. D., 1989, ApJ, 338, 244
Goddi C., Moscadelli L., Sanna A., 2011, A&A, 535, L8
Gómez J. F. et al., 2015, ApJ, 799, 186
Gray M., 1999, Philos. Trans. R. Soc. Lond. Ser. A, 357, 3277
Gray M., 2012, Maser Sources in Astrophysics. Cambridge Univ. Press, Cambridge
Gray M. D., Baggott J., Westlake J., Etoka S., 2019, MNRAS, 486, 4216
Green J. A., McClure-Griffiths N. M., 2011, MNRAS, 417, 2500
Hirota T. et al., 2011, ApJ, 739, L59
Hirota T., Tsuboi M., Kurono Y., Fujisawa K., Honma M., Kim M. K., Imai H., Yonekura Y., 2014a, PASJ, 66, 106
Hirota T., Kim M. K., Kurono Y., Honma M., 2014b, ApJ, 782, L28
Hollenbach D., Elitzur M., McKee C. F., 2013, ApJ, 773, 70
Honma M. et al., 2004, PASJ, 56, L15
Keimpema A. et al., 2015, Exp. Astron., 39, 259
Kramer B. H., Menten K. M., Kraus A., 2018, in Tarchi A., Reid M. J., Castangia P., eds, Proc. IAU Symp. Vol. 336, Astrophysical Masers: Unlocking the Mysteries of the Universe. Cambridge Univ. Press, Cambridge, p. 279
Kurtz S., 2018, 42nd COSPAR Scientific Assembly. p. E1.8–14-18
Lekht E. E., Pashchenko M. I., Rudnitskii G. M., Tolmachev A. M., 2018, Astron. Rep., 62, 213
MacLeod G. C. et al., 2018, MNRAS, 478, 1077
Matveenko L. I., Graham D. A., Diamond P. J., 1988, Soviet Astron. Lett., 14, 468
Molinari S., Brand J., Cesaroni R., Palla F., 1996, A&A, 308, 573
Moscadelli L. et al., 2016, A&A, 585, A71
Moscadelli L., Sanna A., Goddi C., 2018, in Tarchi A., Reid M. J., Castangia P., eds, Proc. IAU Symp. Vol. 336, Astrophysical Masers: Unlocking the Mysteries of the Universe. Cambridge Univ. Press, Cambridge, p. 201
Nagai H. et al., 2013, PASJ, 65, 24
Pérez L. M. et al., 2016, Science, 353, 1519
Shimoikura T., Kobayashi H., Omodaka T., Diamond P. J., Matveyenko L. I., Fujisawa K., 2005, ApJ, 634, 459
Simon M., Dutrey A., Guilloteau S., 2000, ApJ, 545, 1034
Sobolev A. M., Gray M. D., 2012, in Booth R. S., Vlemmings W. H. T., Humphreys E. M. L., eds, Proc. IAU Symp. Vol. 287, Cosmic Masers – from OH to H0. Cambridge Univ. Press, Cambridge, p. 13
Sunada K., Nakazato T., Ikeda N., Hongo S., Kitamura Y., Yang J., 2007, PASJ, 59, 1185
Szymczak M., Olech M., Wolak P., Gérard E., Bartkiewicz A., 2018, A&A, 617, A80
Vlemmings W. H. T., Amiri N., van Langevelde H. J., Tafoya D., 2014, A&A, 569, A92
Volvach A. E., Volvach L. N., MacLeod G., Lekht E. E., Rudnitskij G. M., Tolmachev A. M., 2017, Astron. Telegram, 10728
Volvach L. N. et al., 2019a, Astron. Rep., 63, 49
Volvach L. N., Volvach A. E., Larionov M. G., MacLeod G. C., van den Heever S. P., Wolak P., Olech M., 2019b, MNRAS, 482, L90
Volvach L. N. et al., 2019c, A&A, 628, A89

[1]*Joint Institute for VLBI ERIC, Oude Hoogeveensedijk 4, NL-7991 PD Dwingeloo, the Netherlands*
[2]*Mizusawa VLBI Observatory, National Astronomical Observatory of Japan, 2-21-1 Osawa, Mitaka, Tokyo 181-8588, Japan*
[3]*Korea Astronomy and Space Science Institute, 776 Daedeokdae-ro, Yuseong-gu, Daejeon 34055, Republic of Korea*
[4]*School of Natural Sciences, University of Tasmania, Private Bag 37, Hobart, TAS 7001, Australia*
[5]*Xinjiang Astronomical Observatory, Chinese Academy of Sciences, 150 Science 1-Street, Urumqi, Xinjiang 830011, China*
[6]*Astro Space Center, Lebedev Physical Institute, Russian Academy of Sciences, Leninskiy Prospekt 53, Moscow 119333, Russia*
[7]*INAF – Osservatorio Astronomico di Cagliari, Via della Scienza 5, I-09047 Selargius, Italy*
[8]*Centre for Astronomy, Faculty of Physics, Astronomy and Informatics, Nicolaus Copernicus University, Grudziadzka 5, PL-87-100 Toruń, Poland*
[9]*The University of Western Ontario, 1151 Richmond Street, London, ON N6A 3K7, Canada*
[10]*Hartebeesthoek Radio Astronomy Observatory, PO Box 443, Krugersdorp 1740, South Africa*
[11]*Radio Astronomy and Geodynamics Department of Crimean Astrophysical Observatory, Katsively RT-22, Crimea*
[12]*Lomonosov Moscow State University, Sternberg Astronomical Institute, Moscow 119234, Russia*
[13]*National Radio Astronomy Observatory, PO Box O, 1003 Lopezville Rd., Socorro, NM 87801, USA*
[14]*Sterrewacht Leiden, Leiden University, Postbus 9513, NL-2300 RA Leiden, the Netherlands*
[15]*South African Radio Astronomy Observatory (SARAO), 3rd Floor, The Park, Park Road, Pinelands, Cape Town 7405, South Africa*
[16]*Space Research Unit, Physics Department, North West University, Potchefstroom 2520, South Africa*
[17]*National Astronomical Research Institute of Thailand, 260 M.4, T. Donkaew, Amphur Maerim, Chiang Mai 50180, Thailand*
[18]*University of Science and Technology, Korea (UST), 217 Gajeong-ro, Yuseong-gu, Daejeon 34113, Republic of Korea*
[19]*Astronomical Observatory, Ural Federal University, Lenin Ave. 51, Ekaterinburg 620083, Russia*
[20]*Max-Planck-Institut für Radioastronomie, Auf dem Hügel 69, D-53121 Bonn, Germany*
[21]*Netherlands Institute for Radio Astronomy, Oude Hoogeveensedijk 4, NL-7991 PD Dwingeloo, the Netherlands*
[22]*NRAO, 520 Edgemont Road, Charlottesville, VA 22903, USA*
[23]*Instituto de Radioastronomía y Astrofísica, Universidad Nacional Autónoma de México, Apartado Postal 3-72, Morelia 58089, Mexico*
[24]*INAF – Istituto di Radioastronomia and Italian ALMA Regional Centre, via P. Gobetti 101, I-40129 Bologna, Italy*

This paper has been typeset from a TEX/LATEX file prepared by the author.

Downloaded from https://academic.oup.com/mnras/article/491/3/4069/5625785 by INAF Cagliari (Osservatorio Astronomico di Cagliari) user on 19 April 2021